Original

Herzen, J.; Donath, T.; Beckmann, F.; Ogurreck, M.; David, C.; Mohr, J.;
Pfeiffer, F.; Schreyer, A.:

X-ray grating interferometer for materials-science imaging at a low-coherent wiggler source

In: Review of Scientific Instruments (2011) AIP

DOI: 10.1063/1.3662411

X-ray grating interferometer for materials-science imaging at a low-coherent wiggler source

Julia Herzen,[1,2,a)] Tilman Donath,[3,4] Felix Beckmann,[1] Malte Ogurreck,[1] Christian David,[3] Jürgen Mohr,[5] Franz Pfeiffer,[2] and Andreas Schreyer[1]
[1]*Helmholtz-Zentrum Geesthacht, 21502 Geesthacht, Germany*
[2]*Physics Department and Institute for Medical Engineering, Technische Universität München, 85748 Garching, Germany*
[3]*Paul Scherrer Institut, 5232 Villigen PSI, Switzerland*
[4]*Dectris AG, 5400 Baden, Switzerland*
[5]*Institute of Microstructure Technology, Forschungszentrum Karlsruhe, 76021 Karlsruhe, Germany*

(Received 27 May 2011; accepted 29 October 2011; published online 30 November 2011)

X-ray phase-contrast radiography and tomography enable to increase contrast for weakly absorbing materials. Recently, x-ray grating interferometers were developed that extend the possibility of phase-contrast imaging from highly brilliant radiation sources like third-generation synchrotron sources to non-coherent conventional x-ray tube sources. Here, we present the first installation of a three grating x-ray interferometer at a low-coherence wiggler source at the beamline W2 (HARWI II) operated by the Helmholtz-Zentrum Geesthacht at the second-generation synchrotron storage ring DORIS (DESY, Hamburg, Germany). Using this type of the wiggler insertion device with a millimeter-sized source allows monochromatic phase-contrast imaging of centimeter sized objects with high photon flux. Thus, biological and materials-science imaging applications can highly profit from this imaging modality. The specially designed grating interferometer currently works in the photon energy range from 22 to 30 keV, and the range will be increased by using adapted x-ray optical gratings. Our results of an energy-dependent visibility measurement in comparison to corresponding simulations demonstrate the performance of the new setup. © *2011 American Institute of Physics*. [doi:10.1063/1.3662411]

I. INTRODUCTION

Phase-contrast imaging is based on changes in the x-ray wave front caused by the object. This can greatly increase the contrast for low absorbing materials. This imaging modality is well known from visible-light microscopy,[1] but it is quite new in the field of x-ray imaging.[2–8] For a long time, these methods have been practically limited to highly brilliant radiation as it is available at, e.g., synchrotron radiation sources. Recently, the development of grating interferometers extended x-ray phase-contrast imaging even to conventional x-ray tube sources,[9–11] making the grating-based x-ray phase-contrast imaging feasible also at low-coherent second generation synchrotron radiation sources. These radiation sources provide several orders of magnitude more flux than conventional x-ray tubes, but a much lower brilliance than third generation sources such as, e.g., ESRF/France or PETRA III/Germany. These radiation sources often provide sufficient field-of-views for characterizing centimeter sized objects with monochromatic radiation.

The source divergence of a second generation synchrotron radiation source is much larger compared to that of newer third-generation sources. This fact, and the millimeter-sized source in the wiggler, have two important consequences: (1) It makes the beamline extremely interesting for applications on centimeter-sized objects and (2) it leads to a very low spatial coherence in the x-ray beam that makes phase-contrast imaging relying on high spatial coherence practically impossible. The phase-contrast method using a three-grating interferometer has been used with incoherent sources (x-ray tubes and neutrons[10–13]). We have transferred this design to a wiggler beamline and used it to explore the entire role of the source grating and its influence on the phase-contrast imaging, which has not been investigated so far. With the laboratory sources the space between the source and the interferometer is very limited, so no experimental study on the distance of an extended x-ray source can be done using these sources.

In this paper, we present a three-grating x-ray interferometer setup that was built in cooperation with Paul Scherrer Institut (Switzerland), TU München and Karlsruhe Institute of Technology (KIT) (Germany), and installed at the materials-science beamline W2 (HARWI II) operated by the Helmholtz-Zentrum Geesthacht (HZG) at the storage ring DORIS (DESY, Germany). This is the first grating interferometer setup at a second generation synchrotron storage ring utilizing three gratings and serves as proof of principle of this geometry using a distant wiggler source with a large source size. Based on visibility simulations the influence of the distant wiggler source was investigated and compared with measured values.

The interferometer consists of a source grating G_0, a phase grating G_1, and an analyzing grating G_2. The horizontal source size in the wiggler is ~1.7 mm, resulting in a too small lateral coherence as required for a two grating setup. To produce enough lateral coherence one can, either work with a small aperture or use an absorbing source grating G_0.[9] We favored the latter, as it provides more flux and a sufficient field of view for centimeter sized objects at the same time.

a)Electronic mail: julia.herzen@ph.tum.de.

By keeping the inter-grating distances fixed we can switch between the different fractional Talbot orders easily by changing the photon energy that increases or decreases the phase-contrast sensitivity without mechanical changes on the interferometer.

In the field of materials sciences the grating interferometer imaging method has not yet been widely used. We believe, however, that the materials characterization can highly profit from the three signals provided by the grating interferometer simultaneously.[14,15] The grating interferometer combines the benefits of spatially resolved structure information of x-ray radiography with the complementary phase-contrast signal, and the dark-field signal allowing to visualize porosity and precipitations below the spatial resolution of the imaging system.

II. MATERIALS AND METHODS

A. Beamline parameters

The grating interferometer has been installed at the wiggler beamline W2. This beamline is situated at the storage ring DORIS III and operated by the HZG in cooperation with DESY since 2006 as a high energy materials science beamline. The technical details of the beamline and the absorption tomography experiment have been published by Beckmann *et al.*.[16,17]

A double-crystal monochromator with vertical beam reflection provides a wide beam up to 70 (horizontal) × 8 (vertical) mm^2 making the beamline particularly suitable for tomographic imaging. Different pairs of crystals are used in Laue-Laue and Laue-Bragg geometry to vary the photon energy spectrum.[18–20]

The main characteristics of the beamline W2 are listed in the Table I. The only optical components considered in the flux calculation were the monochromator crystals. Due to the Laue geometry the two 0.7 mm thick silicon (111) crystals each reduces the flux by a factor of 0.5, when no bending is assumed.

Figure 1 shows a schematic of the beamline consisting of the wiggler, an optics hutch with the monochromator tank, the 1st experimental hutch with the setups of tomography and diffraction experiments, the 2nd experimental hutch with a high pressure cell, and the control hutch. The tomography experiment, where the grating interferometer was installed, is situated 48 m away from the wiggler. The beam direction is used as the positive z direction in the following.

TABLE I. Source characteristics of the beamline W2. The integrated flux is calculated using XOP software and given at the sample position through a 1 × 1 mm^2 aperture at 100 mA ring current and a wiggler gap of 20 mm. Influences of additional optical components like crystals are also considered.

Parameter	Unit	
DORIS III		
Positron energy	GeV	4.45
Positron current	mA	140–170
Source size (horizontal) σ_x	mm	1.797
Source size (vertical) σ_z	mm	0.514
Wiggler W2		
Total length	m	4
Period length	mm	110
Number of periods		35
Minimal gap	mm	14
Peak field B_0	T	1.98
K		20.3
Critical energy	keV	26.7
Filters		
Carbon	mm	3(permanent)/7 (variable)
Copper	mm	1.0/2.0
Monochromator		Double-crystal Si-111 (bent Laue) and Si-111 (Bragg), in vacuum
Beam size (max)	mm	70 (horizotal) × 4 (vertical)
Energy range	keV	20–180
Integrated flux	ph/s/mm^2	2.2 × 10^{15}
Flux at 20 keV	ph/s/mm^2/(0.1% BW)	1.6 × 10^{10}
Flux at 30 keV	ph/s/mm^2/(0.1% BW)	7.5 × 10^{10}

B. Signal formation

An x-ray grating interferometer for radiation sources with low lateral coherence consists of three gratings: an absorbing source grating G_0, a phase grating G_1, and an absorbing analyzer grating G_2. The absorbing source grating G_0 with a period p_0 divides the large x-ray source into small mutually incoherent line sources. The phase grating G_1 with the period p_1 introduces a phase shift of π on the incoming wave field that leads to an interference pattern of period p_2 downstream the grating G_1. We call the distance between the gratings G_0 and G_1 l, and the G_1-to-G_2 distance d. As the period p_2 is too small to be directly resolved with an x-ray detector, the absorbing analyzer grating G_2 and a Moiré phase-stepping technique are used.[21] With this method one can measure the refraction of the x-ray beam caused by an object by detecting the displacement of the Moiré pattern.

The grating interferometer obtains three different contrast information: δ and β of the sample's complex refractive index $n = 1 - \delta + i\beta$, and its ability to scatter incoherently the penetrating x-rays.[14] The first one is the conventional x-ray attenuation which is associated with the imaginary part of the complex refractive index β and is measured in form of

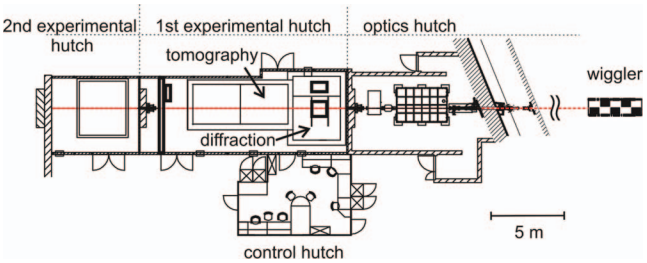

FIG. 1. (Color online) Schematic of the beamline W2 consisting of the wiggler, optics hutch with the monochromator tank, the 1st experimental hutch with tomography and diffraction setups, and the 2nd experimental hutch with a high pressure cell operated by Geoforschungszentrum Potsdam. The red dashed line represents the beam path.

the linear attenuation coefficient μ of the x-rays. The second is the phase shift Φ (Ref. 21) introduced by the object to the x-ray wave field and resulting in a refraction of the beam by an angle α in x-direction. This angle is correlated with the differential phase shift $\partial\Phi/\partial x$ and to the decrement of the refractive index δ by

$$\alpha(x) = \frac{\lambda}{2\pi}\frac{\partial\Phi}{\partial x} = \int_0^{d_{obj}} \frac{\partial\delta}{\partial x}\mathrm{d}z, \tag{1}$$

with λ representing the x-ray wavelength, and d_{obj} being the thickness of the object. The third signal, the so-called *dark-field signal*, can be described as a reduction of the visibility of the interference fringes caused by a beam spread from small angle scattering in the sample.[14,22,23] This spread is connected to a material specific linear diffusion coefficient ϵ, depending on the total scattering width σ and the sample thickness Δz

$$V(x) = \exp\left(\frac{-2\pi^2 p^2}{d^2}\right)\int \epsilon\Delta z, \tag{2}$$

with p the period of the interference pattern and d the distance between the phase grating G_1 and the analyzing grating G_2.

C. Grating interferometer geometry

In case of a parallel-beam illumination a grating G_1 of period p_1 produces interference fringes at fractional Talbot distances

$$D_n = n\frac{p_{1,e}^2}{2\lambda}, \tag{3}$$

with the Talbot orders $n = 0, 1, 2, \ldots$ and the period of the interference pattern behind G_1 $p_{1,e}$, that corresponds to the effective period of grating G1 which can be defined as

$$p_{1,e} = \frac{p_1}{\eta}, \tag{4}$$

with $\eta = 2$ in our case for a π-shifting phase grating. The maximum visibility of the interference pattern occurs at odd Talbot orders ($n = 1, 3, 5, \ldots$).

In case of spherical waves the Talbot distances rescale with a magnification factor M that can be calculated from the distances l and d between the gratings (compare Figure 2) by

$$M = \frac{l+d}{l}, \tag{5}$$

TABLE II. Properties of the interferometer gratings. The gold lines of the gold gratings G_0 and G_2 absorb 90% of the incoming radiation (depending on the photon energy) and the two phase gratings G_1 are optimized for the given optimal x-ray energies inducing a phase shift of π. The duty cycle (DC) of the gold gratings are a trade-off between higher visibility at higher DCs and significant intensity loss. The DC of the phase grating has a very strong influence on the intensity distribution downstream the beam propagation direction and ideally needs to be optimized for every application.

Grating	Period p (μm)	Height h (μm)	Optimal x-ray energy E_{ph} (keV)	Duty cycle DC $\pm$ std
Phase grating G_1#1	4.33	35	27.3	0.42 ± 0.02
Phase grating G_1#2	4.33	54	42.1	0.54 ± 0.04
Source grating G_0	22.29	47	30	0.7
Analyzer grating G_2	2.40	30.8	25	0.5

thus the scaled Talbot distances d_n are determined by

$$d_n = M\, D_n, \tag{6}$$

representing a geometrically magnified projection of G_1 onto G_2 illuminated by a virtual source point in G_0.

The period p_2 of the absorbing analyzer grating G_2 must be chosen equal to the effective period of the phase grating G_1 scaled by the magnification factor M. Choosing the period p_0 of the source grating G_0 according to Refs. 9 and 24 as

$$p_0 = \frac{l}{d}\, p_2, \tag{7}$$

well-defined interference fringes will be produced in the plane of the analyzer grating G_2.

The source and the phase grating are produced at Paul Scherrer Institut (PSI) by wet etching into silicon and electroplating of gold.[25] The analyzer grating is manufactured by KIT using the LIGA process.[26] The periods and the depths of the gratings are listed in Table II. The gold gratings G_0 and G_2 are usable in the energy range below the given energy (absorption of 90% at the given energy) and the two phase gratings G_2 are optimized for the given design energies. Above the design energy of the gold gratings the interference pattern visibility decreases, as the grating absorption becomes

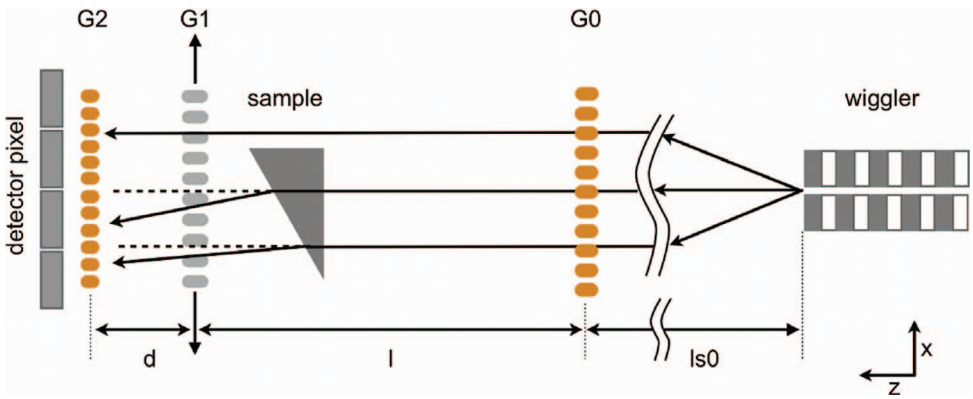

FIG. 2. (Color online) Scheme of grating interferometer at Beamline W2. The interferometer consists of source grating (G_0), phase grating (G_1), and analyzer grating (G_2).

insufficient. In the same way the use of the phase grating G_1 at its design energy increases the visibility, since then the phase shift induced by the grating is almost π. By changing the x-ray energy we can work at different Talbot orders with the same interference geometry. The corresponding Talbot x-ray wavelengths can be derived from Eq. (3) and is given by

$$\lambda_n = nM\frac{p_{1,e}^2}{2d_n}, \tag{8}$$

where n is the odd fractional Talbot order ($n = 1, 3, 5, 7, 9, \ldots$), corresponding to x-ray wavelengths of 0.8, 2.4, 4.0, 5.6, 7.2, $\ldots \times 10^{-11}$ m or photon energies of 152, 51.4, 30.8, 22.0, 17.1, $\ldots$ keV, $p_{1,e}$ is the effective period of the phase grating G_1, and d_n is the fractional Talbot distance scaled by the magnification factor according to Eq. (6).

The total length of the interferometer is 3.32 m with the inter-grating distances $G_0 - G_1 = 3.00$ m, and $G_1 - G_2 = 0.32$ m. Due to the comparably large source size and distance between the specimen and the detector (>0.32 m to fit the interferometer) the best achievable spatial resolution of our imaging system is 15–20 μm. The maximum field of view in the horizontal direction is currently limited by the size of G_0 to 30 mm. The maximum vertical size of the field of view is limited by the monochromator crystals to 4 mm.

D. Image acquisition

The x-ray camera consisted of an ~580 μm thick $CdWO_4$ scintillator lens-coupled to a CCD camera. The PL09000 CCD camera (Finger Lakes Instrumentations, USA) had an active area of 3056×3056 pixels, and a pixel size of 12 μm were used. Taking the magnification by the lens system into account the x-ray camera had an effective pixel size of 10 μm during our experiments. In full frame operation the CCD digitizes with 16 bit at 10 MHz (true dynamic range ≈ 13 bit). The typical exposure times were between 0.3 and 10.0 s per image with a full frame read-out time of 1 s.

For each projection a so-called phase-stepping scan was recorded, in which a set of images at different positions of the phase-stepping grating (in our case the grating G_1) was taken. As we are interested in the performance of the grating interferometer, no sample was in the beam. During the phase-stepping scan 16 phase steps of the grating G_1 over two periods of the interference pattern were recorded and at each position a picture was taken. To calculate the projections from the phase-stepping scan we followed the procedure described in Refs. 14 and 21.

E. Simulation and measurement of visibility

The quality of a grating interferometer can be described by the visibility of the interference fringes, which is described by $V = (I_{max} - I_{min})/(I_{max} + I_{min})$, with I_{max} and I_{min} representing the maximum and minimum measured intensity of the detected interference pattern. Here the visibility is calculated using the 0th and the 1st Fourier coefficients of the intensity oscillation as[14]

$$V = \frac{|a_1|}{|a_0|}. \tag{9}$$

To simulate the visibility of the Moiré fringes produced by the interferometer, we perform the calculations for wave propagation assuming a plane wave setup and rescale the result to the spherical wave setup. By means of the Huygens-Fresnel principle the x-ray wave propagation can be described as a convolution of a wave function $\Phi(x, y, z_0)$ with a propagator function $H_z(x, y)$ where z is the propagation direction.[27,28] For a monochromatic plane wave, the wave function is given by $\Phi(x, y, z_0) = E_0\exp(i2\pi z_0/\lambda)$ and the propagation function

$$H_z(x, y) = \frac{\exp(i2\pi z/\lambda)}{i\lambda z}\exp(i\pi/\lambda z)(x^2 + y^2). \tag{10}$$

The x-ray wave front after a distance $z = z_0 + \Delta z$ in real space can easily be calculated in Fourier space as

$$\Phi(x, y, z) = \mathcal{F}^{-1}\{\mathcal{F}\Phi(x, y, z_0) \times \mathcal{F}H_z(x, y)\}, \tag{11}$$

where $\mathcal{F}\Phi(x, y, z_0)$ represents the 2D Fourier transform of the x-ray wave function at z_0, $\mathcal{F}^{-1}$ denotes the inverse Fourier transform operator, and $\mathcal{F}H_z(x, y)$ is the Fourier representation of the propagation function.

Every object in the x-ray beam can be described by its complex, energy-dependent transmission function $T_\lambda(x, y)$, that describes the distribution of the complex refraction index in the sample in the plane $z = z_{obj}$ and is valid for very thin objects. The wave front directly downstream the object in the plane $z_{obj} + \epsilon$, with ϵ representing a very small distance, is thus given by multiplication in real space or a convolution in Fourier space of the incident wave function by the transmission function of the object

$$\Phi(x, y, z_{obj} + \epsilon) = \Phi(x, y, z) \times T_\lambda(x, y). \tag{12}$$

The use of the Fresnel-Kirchhoff equation in Fourier space and of the paraxial approximation allows fast simulations of an x-ray imaging setup. This sort of simulations does not consider any partial coherence in case of a finite source size or energy bandwidth. All calculations were made assuming a monochromatic incoming plane wave at the sample position. This assumption is valid, as the distance between the source in the wiggler and the sample plane is large (48 m) compared to the wavelength.

We describe our setup with a radiation source situated in the G_0 plane and producing a monochromatic, plane wave front that is shifted in phase by G_1 exactly by a factor of π (please note that the phase shift is only exactly π at the design energy of the grating G_1) and producing a Moiré pattern in the plane of G_2. The calculations of the visibility were performed for different x-ray energies for the setup at the beamline W2 using MATLAB. The simulated results were compared to the measured visibility values for the corresponding energies.

III. RESULTS AND DISCUSSION

For both phase gratings G_1 #1 and #2, the visibility was measured as a function of the photon energy from 16 keV up to 60 keV in steps of 0.5 keV. The visibility was calculated for each projection using Eq. (9). The calculated visibility V was then plotted against the photon energy. At each energy a phase scan with 16 phase steps over 2 periods of the interference pattern was performed, taking images

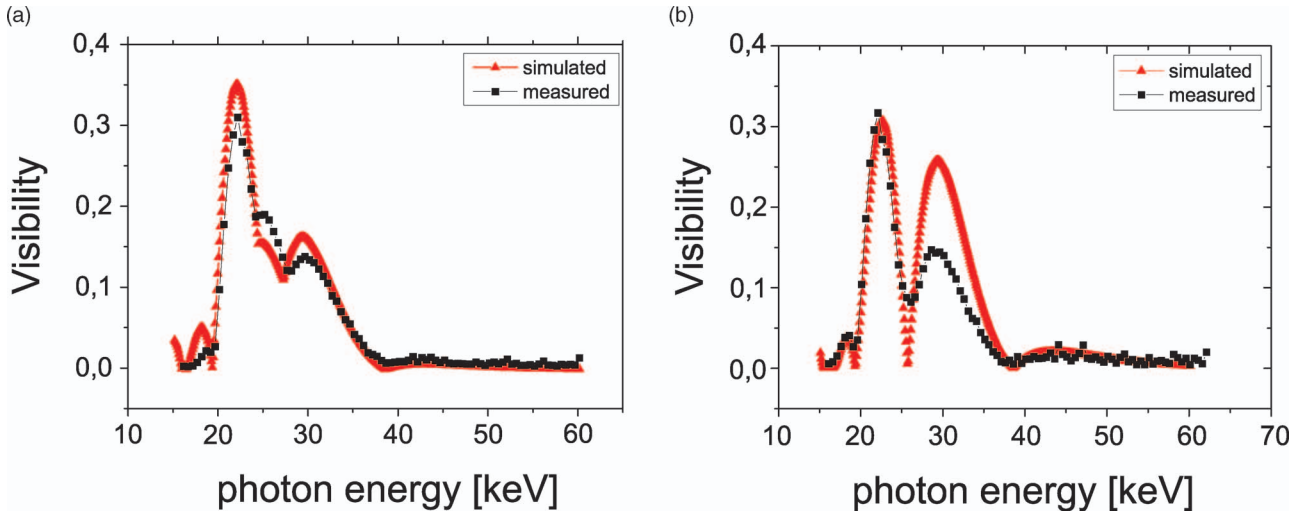

FIG. 3. (Color online) Visibility as a function of photon energy for the phase gratings G_1#1 (a) and G_1#2 (b). The measured visibility with changing photon energy is plotted with black squares, the results of a simulation with red triangles. The maxima of visibility occur at the Talbot energies. The visibility of the grating #1 shows an additional peak at a forbidden 6th fractional Talbot order at 25 keV that is visible due to the duty cycle deviating from 0.5.

at each step. The exposure times varied during the energy scan to avoid overexposure of the detector at higher x-ray energies with higher photon flux. During further data analysis, the mean value of visibility averaged over 200×100 pixels in the center of the projections was calculated and plotted together with the simulated values against x-ray energy in Figures 3(a) and 3(b).

The plots in Figure 3 show the same shape for the measured and the simulated visibility. The phase grating G_1 #1 shows three significant visibility peaks: at 22 keV, at 25 keV, and at 30 keV. The peaks at 22 keV and at 30 keV correspond to the 7th and the 5th fractional Talbot orders. The additional peak at 25 keV corresponds to the 6th fractional Talbot order, which should not be observed for a G_1 with a duty cycle of 0.5. The other phase grating #2 does not show the 6th fractional Talbot order peak at 25 keV, which is due to its duty cycle being close to the optimum value of 0.5. The absolute values at the peak energies in the simulations deviate slightly from the measured values, since the calculations were made for ideal gratings and a plane wave field setup, which were smoothed by a smoothing factor of 20%. In the plot in Figure 3(b) the calculated visibility between the two maxima is lower than the measured one. This deviation can be explained by the high dependence of the calculations on the duty cycle (DC = ratio between the grooves and bars of a grating) of the phase grating G_1 as can be seen from the plot in (a) of the same figure. The DC deviation of all phase gratings is in the range of several percent but it leads to an additional visibility peak for the grating G_1 #1.

The decrease of the visibility, which can be observed towards higher x-ray energies, is due to the fact that the x-ray transmission through both gold gratings G_0 and G_2 increases. This fact leads to a significantly reduced visibility of the Moiré pattern that could be reproduced by the simulations. Nevertheless, the result in Figure 3(a) points out that the grating G_1 #1 can be used in a large freely choosable energy range from 20 keV to 30 keV without mechanical changes on the interferometer.

The Talbot energies resulting from the Talbot wavelengths in Eq. (8) were correctly calculated with the assumption of the slits in G_0 acting as secondary sources in the G_0 plane. If the source point in the wiggler would determine the Talbot orders, they would be at significantly different x-ray energies: the 7th fractional Talbot order at 24.2 keV, the 6th fractional Talbot order at 28.4 keV, and the 5th fractional Talbot order at 33.9 keV. Additionally, the simulated visibility peak positions reproduced in good agreement the measured peak positions.

IV. CONCLUSIONS

The experimental results as well as the simulations showed that the influence of the distant wiggler source on the grating interferometer can be neglected. Furthermore, our work demonstrated experimentally that designing a three-grating interferometer for a parallel-beam geometry with a distant source is equivalent to calculating all geometries with the assumption of a virtual source in the plane of the source grating. This implies that the actual source (in our case in the wiggler) does not influence the Talbot effect, but has only an influence on the image formation (e.g., geometrical magnification of the specimen). This fact has not been demonstrated so far. All reported interferometer designs were either two-grating setups at a parallel beam geometry or three-grating laboratory setups at a fan beam geometry, but a source grating close to the actual source. Our results will help further theoretical investigations to consider correctly the role of the source grating. The setup at the beamline W2 is comparable to a setup at a conventional non-coherent x-ray tube, except of a much higher photon flux allowing monochromatic illumination. Only the spatial resolution of the grating setup is limited by the wiggler source. Since the interferometer demands a larger distance between the object and the detector, the image blur caused by the source divergence will increase compared to conventional absorption contrast imaging.

Our results demonstrate that a three-grating setup can be very efficiently used at a low-coherent synchrotron radiation

source. Since this particular phase-contrast method is very tolerant to deviations from the design energy, the new grating setup can be used in the energy range from 20 to 30 keV without any mechanical changes on the interferometer. Only the photon energy needs to be changed, which can be very precisely and reproducibly done using the monochromator. The stability of the method makes it especially suitable for user operation, which is already available to external users of the tomography setup at the beamline W2.[29] The upgrade of the grating interferometer in June 2011 will increase the usable energy range up to 50 keV.

We believe that the newly installed grating interferometer at the materials science beamline W2 is the first step to establish this phase-contrast imaging modality in the field of materials sciences. The materials characterization can strongly benefit from the complementary information gained by using the grating interferometer, when optimizing advanced joining techniques for aluminum and magnesium alloys.

ACKNOWLEDGMENTS

We gratefully acknowledge the grating production by C. Grünzweig (PSI), J. Kenntner, and E. Reznikova (KIT) and the support by O. Bunk (PSI), R. Kirchhof, and H. Burmester (HZG). F. Pfeiffer acknowledges support through the DFG Cluster of Excellence Munich Center for Advanced Photonics and the European Research Council (FP7, Starting Grant No. 240142).

[1] F. Zernicke, Physica **1**, 689 (1934).
[2] U. Bonse and M. Hart, Appl. Phys. Lett. **6**, 155 (1965).
[3] F. Beckmann, U. Bonse, F. Busch, and O. Günnewig, J. Comput. Assist. Tomogr. **21**(4), 539 (1997).
[4] P. Cloetens, W. Ludwig, J. Baruchel, D. van Dyck, J. van Landuyt, J. P. Guigay, and M. Schlenker, Appl. Phys. Lett. **75**, 2912 (1999).
[5] A. Momose, Nucl. Instrum. Methods A **352**, 622 (1995).
[6] A. Momose, S. Kawamoto, I. Koyama, Y. Hamaishi, K. Takai, and Y. Suzuki, Jpn. J. Appl. Phys. **42**, L866 (2003).
[7] A. Momose, Jpn. J. Appl. Phys. **44**, 6355 (2005).
[8] A. Momose, W. Yashiro, Y. Takeda, Y. Suzuki, and T. Hattori, Jpn. J. Appl. Phys. **45**(6A), 5254 (2006).
[9] F. Pfeiffer, T. Weitkamp, O. Bunk, and C. David, Nat. Phys. **2**, 258 (2006).
[10] F. Pfeiffer, C. Kottler, O. Bunk, and C. David, Phys. Rev. Lett. **98**, 108105 (2007).
[11] T. Weitkamp, C. David, C. Kottler, O. Bunk, and F. Pfeiffer, Proc. SPIE **6318**, 63180S (2006).
[12] M. Engelhardt, C. Kottler, O. Bunk, C. David, C. Schroer, J. Baumann, M. Schuster, and F. Pfeiffer, J. Microsc. **232**(1), 145 (2008).
[13] C. Grünzweig, Ph.D. dissertation, Eidgenössischen Technischen Hochschule Zürich, 2009.
[14] F. Pfeiffer, M. Bech, O. Bunk, P. Kraft, E. F. Eikenberry, C. Brönnimann, C. Grünzweig, and C. David, Nature Mater. **7**, 134 (2008).
[15] J. Herzen, T. Donath, F. Pfeiffer, O. Bunk, C. Padeste, F. Beckmann, A. Schreyer, and C. David, Opt. Express **17**(12), 10010 (2009).
[16] F. Beckmann, T. Lippmann, J. Metge, T. Dose, T. Donath, M. Tischer, K. D. Liss, and A. Schreyer, AIP Conf. Proc. **705**, 392 (2004).
[17] F. Beckmann, T. Dose, T. Lippmann, L. Lottermoser, R.-V. Martins, and A. Schreyer, AIP Conf. Proc. **879**, 746 (2007).
[18] G. Illing, J. Heuer, B. Reime, M. Lohmann, R. H. Menk, L. Schildwächter, W.-R. Dix, and W. Graeff, Rev. Sci. Instrum. **66**(2), 1379 (1995).
[19] M. Lohmann, W.-R. Dix, J. Metge, and B. Reime, AIP Conf. Proc. **705**, 1295 (2004).
[20] F. Beckmann, T. Donath, J. Fischer, T. Dose, T. Lippmann, L. Lottermoser, R. V. Martins, and A. Schreyer, Proc. SPIE **6318**, 631810 (2006).
[21] T. Weitkamp, A. Diaz, C. David, F. Pfeiffer, M. Stampanoni, P. Cloetens, and E. Ziegler, Opt. Express **13**, 6296 (2005).
[22] M. Bech, O. Bunk, T. Donath, R. Feidenhans'l, C. David, and F. Pfeiffer, Phys. Med. Biol. **55**(18), 5529 (2010).
[23] W. Yashiro, Y. Terui, K. Kawabata, and A. Momose, Opt. Express **18**(16), 16890 (2010).
[24] K. Patorski, Appl. Optics **25**(14), 2396 (1986).
[25] C. David, J. Bruder, T. Rohbeck, C. Grünzweig, C. Kottler, A. Diaz, O. Bunk, and F. Pfeiffer, Microelectron. Eng. **84**, 11721177 (2007).
[26] E. Reznikova, J. Mohr, M. Boerner, V. Nazmov, and P.-J. Jakobs, Microsyst. Technol. **14**, 16831688 (2008).
[27] J. W. Goodman, *Introduction to Fourier Optics* (Roberts & Company Publishers, Colorado, USA, 2007).
[28] T. Weitkamp, Proc. SPIE **5536**, 181 (2004).
[29] B. Müller, G. Schulz, J. Herzen, S. Mushkolaj, T. Bormann, F. Beckmann, and K. Püschel, Proc. SPIE **7804**, 78040D (2010).